Received 8 July 2021; revised 24 August 2021; accepted 25 August 2021. Date of publication 30 August 2021;
date of current version 13 December 2021. The review of this paper was arranged by Editor D. Misra.

Digital Object Identifier 10.1109/JEDS.2021.3108882

WS_2 Film by Sputtering and Sulfur-Vapor Annealing, and Its *p*MISFET With TiN/HfO_2 Top-Gate Stack, TiN Bottom Contact, and Ultra-Thin Body and Box

TAKUYA HAMADA [1], MASAYA HAMADA [1], SATOSHI IGARASHI [1], TAIGA HORIGUCHI [1], IRIYA MUNETA [1] (Member, IEEE), KUNIYUKI KAKUSHIMA [1] (Member, IEEE), KAZUO TSUTSUI [2] (Senior Member, IEEE), TETSUYA TATSUMI [3], SHIGETAKA TOMIYA [3], AND HITOSHI WAKABAYASHI [1] (Senior Member, IEEE)

1 Department of Electrical and Electronic Engineering, School of Engineering, Tokyo Institute of Technology (Suzukakedai Campus), Yokohama 226-8503, Japan
2 Interdisciplinary Graduate School of Science and Engineering, Tokyo Institute of Technology (Suzukakedai Campus), Yokohama 226-8503, Japan
3 Research Institute for the Earth Inclusive Sensing, Tokyo Institute of Technology (Suzukakedai Campus), Yokohama 226-8503, Japan

CORRESPONDING AUTHOR: T. HAMADA (e-mail: hamada.t.ai@m.titech.ac.jp)

This work was supported in part by the Collaborative Research Chair/Division Program founded by Sony Corporation and in part by Japan Science and Technology Agency Center of Innovation Program (JST COI) under Grant JPMJCE1309.

ABSTRACT A layered polycrystalline WS_2 film is formed by radio-frequency (RF) magnetron sputtering and sulfur-vapor annealing (SVA). Its *p*MISFET is successfully demonstrated with TiN/HfO_2 top-gate stack, TiN contact, and ultra-thin body and box technologies. A WS_2 film with a (002) plane is formed parallel to a substrate surface using RF magnetron sputtering, and its crystallinity is drastically enhanced by the SVA. *I–V* characteristics with *p*-type operation are confirmed in WS_2 MISFETs with a maximum field effect mobility of 1.5×10^{-2} $cm^2V^{-1}s^{-1}$. Therefore, our film-formation method is a promising candidate for *p*MOSFETs in CMOS circuits.

INDEX TERMS Tungsten disulfide (WS_2), *p*MISFET, ultra-high vacuum (UHV), radio-frequency (RF) magnetron sputtering, sulfur-vapor annealing (SVA), TiN top gate, TiN contact, ultra-thin body and box (UTBB).

I. INTRODUCTION

Silicon technology with FinFETs in logic LSIs has been scaled down to the 5-nm technology node [1], [2]. Although nano-sheet and fork-sheet devices have been recently proposed beyond 5 nm, they need thin channels in several-nanometer size, in which a scattering is required to be controlled to enhance a mobility [3]. With respect to the silicon (Si), it has been reported that the mobility decreases with a decrease in the channel thickness due to an increase in the scattering effect by the dangling bonds at Si surface. In contrast, a tungsten disulfide (WS_2) film among a transition metal di-chalcogenide (TMDC) has an atomically thin 2D structure without dangling bond, resulting in high mobility. A calculated high mobility has been reported to be more than 1,000 $cm^2V^{-1}s^{-1}$ for a mono layer [4]. Therefore, WS_2 films as well as films of other TMDCs are expected to be applicable not only to advanced LSIs but also to energy harvesters, displays and sensors [5]–[11].

To obtain an atomically thin WS_2 film with a large area for such applications, the chemical vapor deposition (CVD) method has been investigated, in which a WS_2 film on a 300 mm wafer has been reported [12], [13]. However, this requires a transfer technique to obtain the WS_2 film onto Si substrates, which raises concerns about contamination due to residues during transfer. To avoid unexpected difficulties and to realize large films, sputtering under ultra-high vacuum

(UHV) has been proposed as a physical vapor deposition (PVD) technique [14], [15].

Previously, a combination of sputtering and sulfur vapor annealing (SVA) was used to realize layered-polycrystalline TMDC films with a low carrier density, large area and uniform thickness [16]–[18], resulting in normally off MoS_2 *n*MISFETs [19] and ZrS_2 ambipolar-MISFETs [20]. Compared to MoS_2 and ZrS_2 films, the WS_2 has the advantages of a higher calculated mobility than MoS_2 film and lower mass anisotropy than ZrS_2 film. Recently, we fabricated a WS_2 film by PVD and demonstrated its *p*MISFET consisting of TiN/HfO_2 top-gate stack, TiN bottom contact, and ultra-thin body and box (UTBB) technologies [21].

In this paper, the characteristics of both a WS_2 film and the *p*MISFETs are discussed in detail.

II. EXPERIMENTAL METHODS

A. WS_2 FILM FORMATION

A base material of silicon dioxide (SiO_2) with a 400-nm thickness on a Si substrate was cleaned by a piranha solution. A WS_2 film was formed on the substrate by using an UHV radio frequency (RF) magnetron sputtering tool having a 99.99% purity WS_2 target (Matsurf Technologies Inc.) with a power of 80 W. Here, a WS_2 film was deposited for a deposition time of 160 seconds for transmission electron microscopy (TEM). For other physical measurements, 2.5-nm-WS_2 films were deposited for a deposition time of 60 seconds based on a deposition rate calculated from the TEM results. The distance between the target and the substrate was 150 mm, and sputtering was performed at a substrate temperature of 300°C under an argon pressure of 0.55 Pa. The WS_2 film was annealed at 700°C using sulfur (S) under 100 Pa for 60 min [16].

The atomic-scale structure of the WS_2 film was observed using TEM with an accelerating voltage of 200 keV. An X-ray diffraction (XRD) analysis was performed using a Cu K_α X-ray source operated at 45 kV and 200 mA. Atomic force microscopy (AFM) was performed in the dynamic force microscopy (DFM) mode. The Raman spectroscopy was performed using the laser with a wavelength of 532 nm, and a pseudo-Voigt function was used to describe the Raman spectrum of the WS_2 film. An X-ray photoelectron spectroscopy (XPS) was performed by an Al K_α X-ray source, and spectral fitting was also carried out using the pseudo-Voigt function. The composition ratio of the WS_2 film is defined as follows:

$$C_i = \frac{A_i/\mathrm{RSF}_i}{\sum_j A_j/\mathrm{RSF}_j}, \tag{1}$$

where C_i, A_i and RSF_i are the composition ratio, peak area and relative sensitivity factor of the atom i, respectively. To obtain the Arrhenius plots of resistivity for WS_2 films with and without SVA, the Van der Pauw measurements were performed for $WS_2/SiO_2/Si$ samples with TiN bottom contacts in 1 cm × 1 cm area. Bottom electrodes with titanium-nitride (TiN) film with a thickness of 50 nm were formed by sputtering and wet etching with an ammonia-hydrogen peroxide mixture (APM) with photo resist. After substrate cleaning using acetone and ethanol, 2.5-nm-WS_2 films were formed for a deposition time of 60 seconds.

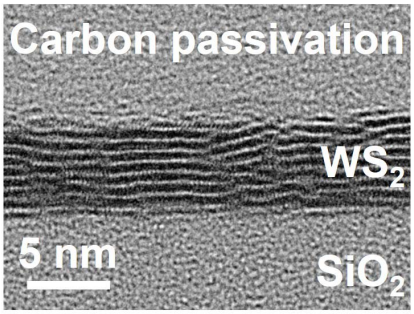

FIGURE 1. Cross-sectional TEM image of WS_2 film sputtered at 80 W using SVA directly on SiO_2/Si substrate.

B. WS_2 MISFET WITH TIN/HFO_2-GATE, TIN CONTACT & UTBB

TiN source and drain (S/D) electrodes with a thickness of 50 nm were fabricated on 87-nm-SiO_2/p^+-Si substrate, which is suitable for UTBB and silicon on thin BOX (SOTB) [22], [23]. A 2.5-nm-WS_2 film was formed by sputtering for 60 seconds and SVA. A 17-nm-HfO_2 gate insulator was deposited by an atomic-layer deposition (ALD) at 300°C with tetrakis(dimethyl)-aminohafnium (TDMAH) and H_2O precursors. Here, ALD-insulator films on the TMDC film deposited by the magnetron sputtering have good coverage even without any functionalization at the surface of the TMDC film, because there are appropriately active sites at grain boundaries of the surface. [19], [24]. A 60-nm-SiN sidewall was formed by lift-off, just after active area definition with lithography and etching. A top gate electrode with an 80-nm-TiN film and contact metals with 40-nm-TiN films were formed with sputtering and lift-off, respectively. Finally, an SiO_2 film on the backside of the substrate was etched with buffered hydrogen fluoride (BHF).

III. RESULTS AND DISCUSSION

A. WS_2 FILM BY SPUTTERING AND SVA

From a cross-sectional TEM image of the WS_2 film formed by sputtering and SVA shown in Fig. 1, a layered structure parallel to the SiO_2 surface is confirmed. In addition, an out-of-plane XRD pattern is shown in Fig. 2. (002) plane peaks in WS_2 films with and without SVA are observed, which indicate that layered WS_2 film was formed during the sputtering process. A lattice constant with the (002) plane from the diffraction peak was changed from 0.67 to 0.64 nm during the SVA. It is speculated that this is because of a sulfur compensation by the SVA. To examine the morphology and roughness of the film surfaces, AFM images after PVD and SVA are shown in Figs. 3(a) and (b), respectively. Although some residues on the film are found after SVA due to the residual S which may be formed by cooling of the vaporized

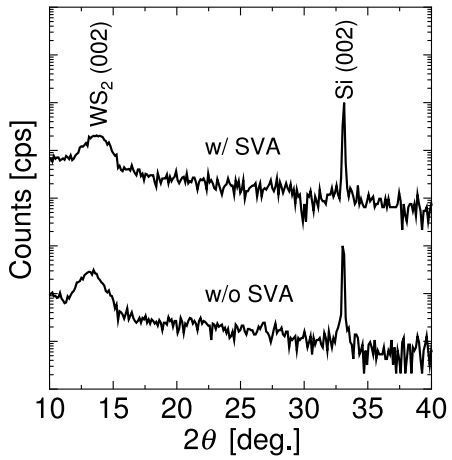

FIGURE 2. XRD patterns of WS_2 films at 80 W with and without SVA. (002) plane peaks are observed in parallel to substrate surface.

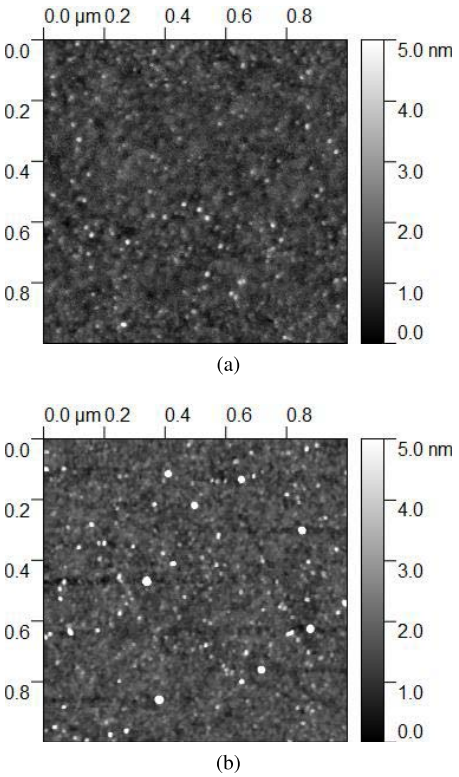

FIGURE 3. AFM images of WS_2 films at 80 W after (a) PVD and (b) SVA. Root mean square values of roughness are 0.40 and 0.64 nm, respectively.

sulfur, a smooth surfaces are observed with the root mean square (RMS) values of 0.40 and 0.64 nm after PVD and SVA, respectively. Moreover, this residue is removed during an early stage of the following ALD process at 300°C under low pressure.

To confirm improvement of crystallinity by SVA, the Raman spectra are shown in Fig. 4. Three peaks are confirmed and their intensities are significantly enhanced by SVA. Here, these peaks include E^1_{2g} mode as the in-plane

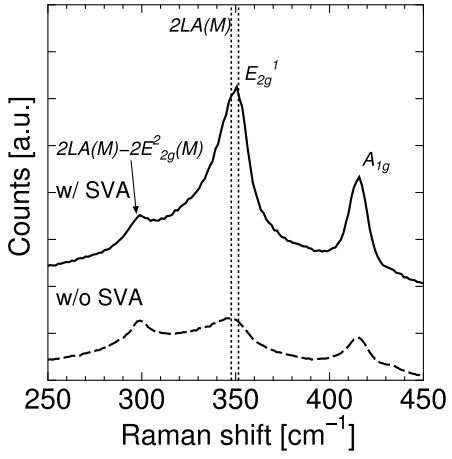

FIGURE 4. Raman spectra of WS_2 films at 80 W with and without SVA. Peak intensities are significantly enhanced by SVA.

vibration of W-S, A_{1g} mode as the out-of-plane vibration of S and a second-order Raman resonance involving the longitudinal acoustic phonons (2LA(M)). It is speculated that S-vacancies in the WS_2 film are compensated by SVA.

To investigate the differences in the chemical composition ratio of the films between before and after SVA, XPS analyses were performed as shown in Fig. 5. In Fig. 5(a), the W 4*f* peaks are found consisting of W-S and also W-O bonding as which the PVD WS_2 film can be oxidized due to an exposure in the air. In Fig. 5(b), the S 2*p* peaks are found consisting of S-W and also S-S bonding. The S/W composition ratio in the WS_2 film calculated from the W-S and S-W peak areas increased from 1.60 to 1.94 because of the SVA. Therefore, it is considered that the S vacancies in the film are effectively compensated. In addition, shifts in binding energy peaks of W $4f_{7/2}$ and S $2p_{3/2}$ toward the negative direction were observed after SVA. It has been reported that sulfur vacancies in the WS_2 film induce a shift of the Fermi level toward the conduction band minimum, because of an n-type doping effect from a theoretical calculation [25]. In addition, from experimental results, shifts in binding energy peaks of W $4f_{7/2}$ and S $2p_{3/2}$ in the same direction have been confirmed [26], [27]. Therefore, our result indicates that the Fermi level shifts away from the conduction band minimum, which is consistent with the S vacancies compensation because it reduces the carrier electrons.

To discuss the difference in the electrical characteristics of the film with and without SVA, Arrhenius plots of resistivity are shown in Fig. 6. Here, resistivity values at above 200 K and 90 K with and without SVA were respectively selected because of the Ohmic *I*–*V* characteristics rather than the Schottky ones. The resistivities in both films decrease with an increase in temperature, clearly demonstrating semiconducting characteristics. It is modeled using the thermally activated transport equation [28]–[30]:

$$\rho = \frac{1}{\sigma} = \frac{1}{qn(T)\mu(T)} = \frac{1}{\sigma_0(T)} \exp\left(\frac{E_a}{k_B T}\right) \qquad (2)$$

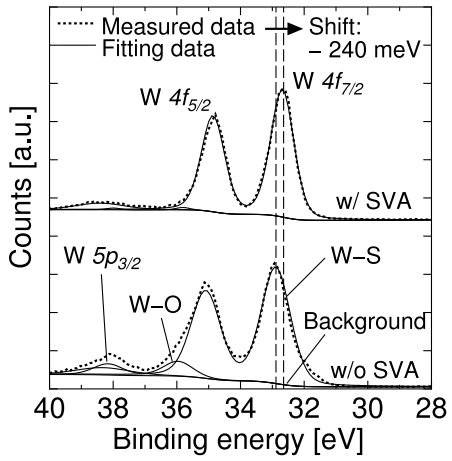

(a)

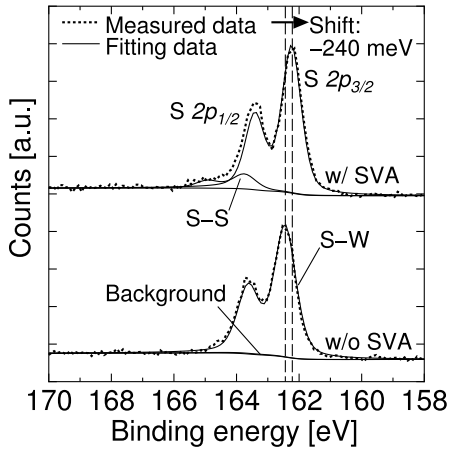

(b)

FIGURE 5. XPS spectra of (a) W 4*f* and (b) S 2*p* in PVD WS_2 films at 80 W with and without SVA. The black dotted and solid lines represent measured and fitted spectra, respectively.

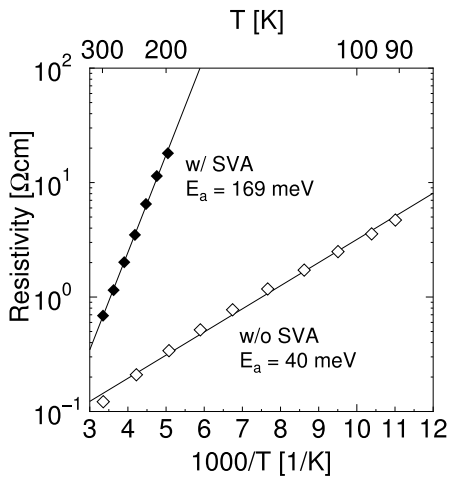

FIGURE 6. Arrhenius plots of resistivity in WS_2 films with and without SVA.

where E_a, k_B, and σ_0 are the activation energy, the Boltzmann constant, and a pre-factor depending on the temperature, respectively. The activation energy increases from 40 to 169 meV because of SVA. It is concerned that the low activation-energy and resistivity of the film without SVA are attributed to high density of S vacancies, which induces n-type carrier generation [25]. S compensation because of SVA successfully performed the Fermi level shift away from the conduction band minimum. This consideration is consistent with the discussion on the XPS results.

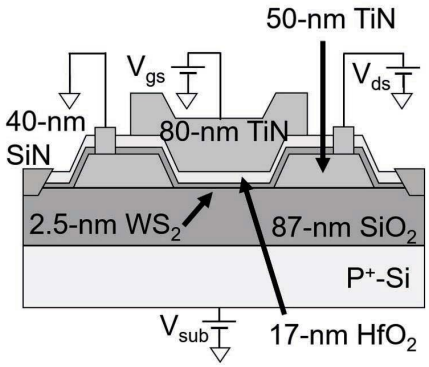

FIGURE 7. Cross-sectional schematic diagram of top-gate WS_2 MISFET with UTBB.

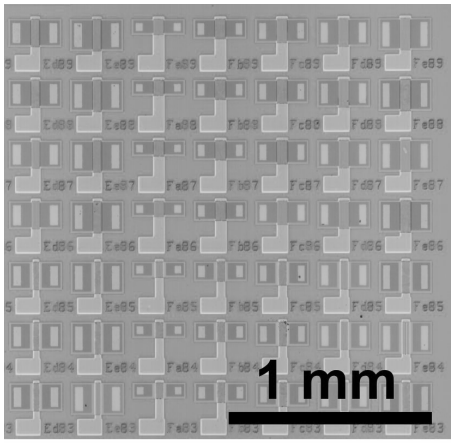

FIGURE 8. Optical top view of WS_2 MISFET array, where channel length and width are varied.

B. WS_2 pMISFETS

A cross-sectional schematic illustration of a fabricated WS_2 MISFET and a top optical image of the FET array are shown in Figs. 7 and 8, respectively. The WS_2 channel is contacted with the bottom TiN S/D metals with an overlap of 5 μm. An RMS value of 1.7 nm was confirmed at a surface of HfO_2/WS_2 film from the AFM, which is the similar value with that in previous reports [19], [24].

To confirm the dielectric properties of the top-HfO_2 and the bottom-SiO_2 films, the I_d, I_s, I_g, and I_{sub} values as a function of V_{gs} are compared, whose characteristics were measured in the WS_2 *p*MISFET with $L_{ch} = 10$ μm and $W_{ch} = 80$ μm at $V_{ds} = -1.0$ V (Fig. 9). I_g and I_{sub} values are about three-order smaller than the I_d one. Therefore,

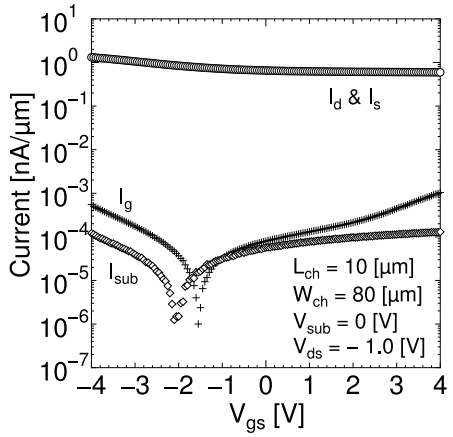

FIGURE 9. I_d–, I_s–, I_g– and I_{sub}–V_{gs} characteristics of WS_2 *p*MISFET with L_{ch} of 10 μm and W_{ch} of 80 μm at a V_{ds} value of −1.0 V. I_g and I_{sub} values are effectively reduced.

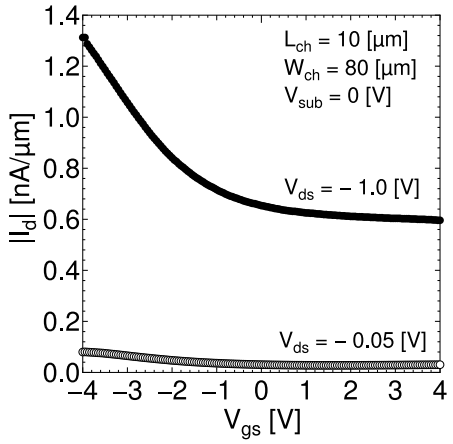

FIGURE 10. I_d–V_{gs} characteristics of WS_2 *p*MISFET with L_{ch} of 10 μm and W_{ch} of 80 μm at V_{ds} values of −0.05 and −1.0 V. *P*-type characteristics are successfully observed.

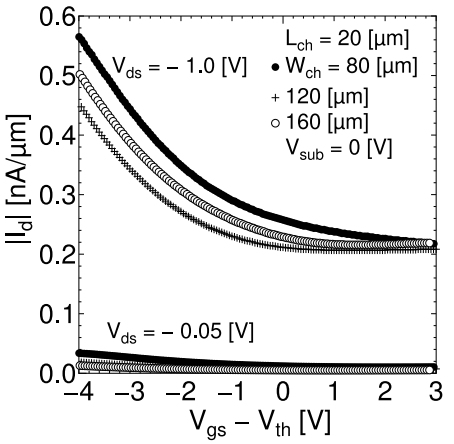

FIGURE 11. I_d–V_{gs} characteristics of WS_2 *p*MISFET with L_{ch} of 20 μm and W_{ch} of 80, 120 and 160 μm at a V_{ds} value of − 1.0 V and V_{sub} value of 0 V.

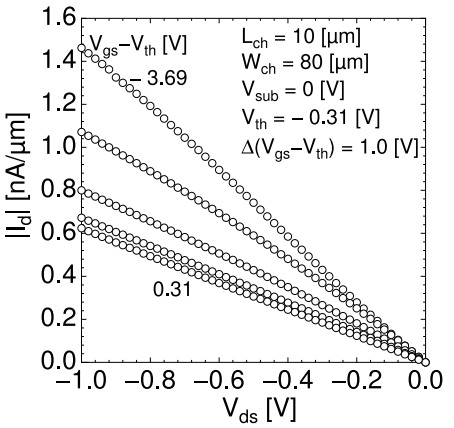

FIGURE 12. I_d–V_{ds} characteristics of WS_2 *p*MISFET with L_{ch} of 10 μm and W_{ch} of 80 μm. Values of V_{gs} – V_{th} were varied from 0.31 to −3.69 V.

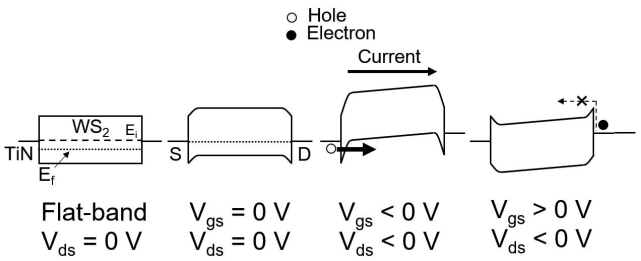

FIGURE 13. Band diagrams under different gate and drain voltages with Schottky-barrier FET model for WS_2 channel.

the top-HfO_2 and bottom-SiO_2 films of the device show understandable behavior as an insulator.

In order to evaluate the drive current and operation type of the FET, I_d–V_{gs} characteristics at V_{ds} values of −0.05 and −1.0 V in Fig. 10 are confirmed. Although a SS value is comparatively larger than expected due to a leakage current at larger negative V_{ds} values, *p*-type characteristics are obviously observed. Here, interface-characteristics at HfO_2/WS_2 and WS_2/SiO_2 are required to be improved to enhance the SS value. Additionally, Fig. 11 shows the variation in I_d–V_{gs} characteristics for several W_{ch}. Here, threshold voltage, V_{th}, values are extracted by an intercept of an extrapolated straight line along the maximum slope of the g_m–V_{gs} curve, described below, to the V_{gs}-axis. I_d values normalized by W_{ch} show only a small difference in the off state at higher positive V_{gs} values, indicating that the leakage current at the channel width edges is negligible because of successful passivation through encapsulation with the SiN sidewall film for the WS_2 film. The I_d–V_{ds} characteristics, shown in Fig. 12, indicate that gate voltage modulation is successfully performed.

P-type transfer characteristics, as discussed above, can be explained by the Schottky-barrier FET model [31], as shown in Fig. 13. We assume that a high work function of approximately 4.7 eV in TiN contacts is relatively closer to the valence band maximum of the WS_2 film rather than the conduction band minimum [32]. In addition, the Fermi level

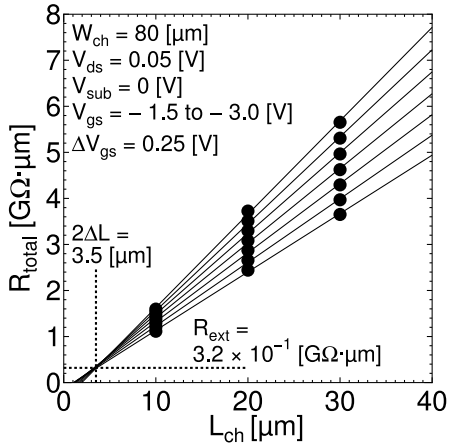

FIGURE 14. R_{total} as function of L_{ch} with W of 80 μm at a V_{ds} value of −0.05 V and a V_{sub} value of 0 V. R_{ext} and $2\Delta L$ are 0.32 GΩμm and 3.5 μm, respectively.

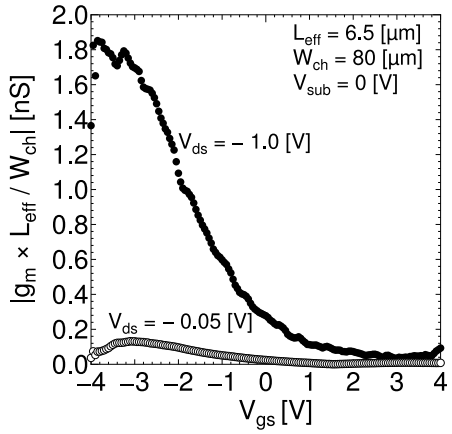

FIGURE 15. g_m–V_{ds} characteristics normalized by W_{ch} and L_{eff} to avoid parasitic resistance.

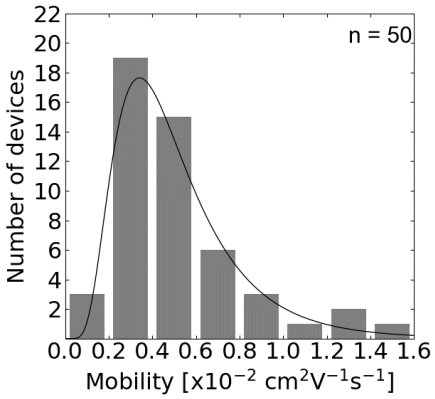

FIGURE 16. Histogram of field effect mobilities in WS_2 *p*MISFETs. Black curve shows the log-normal distribution.

in the WS_2 film is located below the intrinsic level because of the improvement in crystallinity through the S compensation using SVA. Under these discussions, holes contribute to the current at a negative V_{gs}, because of the thinner Schottky barrier, rather than electrons.

Finally, to evaluate the intrinsic drivability of holes in FETs, the parasitic resistance R_{ext} and effective channel length L_{eff} are extracted by the Terada method [33], based on the dependence of resistance on the L_{ch} value, as shown in Fig. 14. An R_{ext} value of 0.32 GΩ μm and a $2\Delta L$ value of 3.5 μm were calculated from $L_{eff} = L_{ch} - 2\Delta L$. The $g_m - V_{gs}$ characteristics normalized by L_{eff} and W_{ch} without parasitic resistance are shown in Fig. 15. The field effect mobility μ_{FE} is calculated using the abovementioned g_m values. Fig. 16 shows a histogram of μ_{FE} for 50 devices with L_{ch} ranging from 5 to 50 μm and W_{ch} ranging from 80 to 160 μm. A maximum μ_{FE} value of 1.5×10^{-2} $cm^2V^{-1}s^{-1}$ is successfully obtained and log-normal distribution was suitable for this histogram. The WS_2 films in this paper have small grain sizes and, thus, many grain boundary, which make carriers mean free path shorten. Therefore, the electrical performance can be further enhanced by enlarging the grain size and controlling the process conditions.

IV. CONCLUSION

WS_2 *p*MISFETs formed by sputtering and SVA were successfully demonstrated. An atomic layered (002)-oriented WS_2 film was formed parallel to the surface of a substrate by the UHV RF magnetron sputtering. The crystallinity of the film was drastically enhanced by the SVA through compensation of S vacancies. A WS_2 *p*MISFET array was successfully realized by TiN/HfO_2 top-gate stack, TiN contact and UTBB technologies. A maximum μ_{FE} of 1.5×10^{-2} $cm^2V^{-1}s^{-1}$ and the log-normal distribution for 50 devices were obtained. The PVD process is a promising candidate for *p*MOSFETs in CMOS circuits beyond the 5-nm technology node.

ACKNOWLEDGMENT

The authors would like to thank Dr. Takuya Hoshii for the variable discussions and his warm supports. Their measurements were supported by Associate Professor Ken Motokura and Open Facility Center at the Tokyo Institute of Technology.

REFERENCES

[1] H. Wakabayashi *et al.*, "Characteristics and modeling of sub-10-nm planar bulk CMOS devices fabricated by lateral source/drain junction control," *IEEE Trans. Electron Devices*, vol. 53, no. 9, pp. 1961–1970, Sep. 2006, doi: 10.1109/TED.2006.880169.

[2] G. Yeap *et al.*, "5nm CMOS production technology platform featuring full-fledged EUV, and high mobility channel FinFETs with densest 0.021μm^2 SRAM cells for mobile SoC and high performance computing applications," in *Proc. Int. Electron Devices Meeting*, San Francisco, CA, USA, 2019, p. 1–4, doi: 10.1109/IEDM19573.2019.8993577.

[3] K. Uchida and S.-I. Takagi, "Carrier scattering induced by thickness fluctuation of silicon-on-insulator film in ultrathin-body metal–oxide–semiconductor field-effect transistors," *Appl. Phys. Lett.*, vol. 82, no. 17, pp. 2916–2918, Apr. 2003, doi: 10.1063/1.1571227.

[4] W. Zhang, Z. Huang, W. Zhang, and Y. Li, "Two-dimensional semiconductors with possible high room temperature mobility," *Nano Res.*, vol. 7, no. 12, pp. 1731–1737, Sep. 2014, doi: 10.1007/s12274-014-0532-x.

[5] M. Mayberry, "The future of compute: How the data transformation is reshaping VLSI," in *Proc. Symp. VLSI Technol. Circuits*, Honolulu, HI, USA, 2020, pp. 1–4, doi: 10.1109/VLSITechnology18217.2020.9265068.

[6] C.-C. Cheng *et al.*, "First demonstration of 40-nm channel length top-gate WS_2 pFET using channel area-selective CVD growth directly on SiOx/Si substrate," in *Proc. Symp. VLSI Technol.*, Kyoto, Japan, 2019, pp. T244–T245, doi: 10.23919/VLSIT.2019.8776498.

[7] W. Wu *et al.*, "Piezophototronic effect in single-atomic-layer MoS_2 for strain-gated flexible optoelectronics," *Adv. Mater.*, vol. 28, no. 38, pp. 8463–8468, Oct. 2016, doi: 10.1002/adma.201602854.

[8] N. Choudhary *et al.*, "Directly deposited MoS_2 thin film electrodes for high performance supercapacitors," *J. Mater. Chem. A*, vol. 3, no. 47, pp. 24049–24054, Oct. 2015, doi: 10.1039/c5ta08095a.

[9] D. Sarker, W. Liu, X. Xiw, A. C. Anselmo, S. Mitragotri, and K. Banerjee, "MoS_2 field-effect transistor for next-generation label-free biosensors," *ACS Nano*, vol. 8, no. 4, pp. 3992–4003, Mar. 2014, doi: 10.1021/nn5009148.

[10] W. Wu *et al.*, "Piezoelectricity of single-atomic-layer MoS_2 for energy conversion and piezotronics," *Nature*, vol. 514, pp. 470–474, Oct. 2014, doi: 10.1038/nature13792.

[11] G. Kogo *et al.*, "A thin film efficient PN-junction thermoelectric device fabricated by self-align shadow mask," *Sci. Rep.*, vol. 10, pp. 1–12, Jan. 2020, doi: 10.1038/s41598-020-57991-y.

[12] C. Huyghebaert *et al.*, "2D materials: Roadmap to CMOS integration," in *Proc. IEEE Int. Electron Devices Meeting*, San Francisco, CA, USA, 2018, pp. 1–4, doi: 10.1109/IEDM.2018.8614679.

[13] I. Asselberghs *et al.*, "Wafer-scale integration of double gated WS2-transistors in 300mm Si CMOS fab," in *Proc. IEEE Int. Electron Devices Meeting*, San Francisco, CA, USA, 2020, pp. 1–4, doi: 10.1109/IEDM13553.2020.9371926.

[14] T. Ohashi *et al.*, "Multi-layered MoS_2 film formed by high-temperature sputtering for enhancement-mode nMOSFETs," *Jpn. J. Appl. Phys.*, vol. 54, no. 4S, Mar. 2015, Art. no. 04DN08, doi: 10.7567/JJAP.54.04DN08.

[15] T. Sakamoto *et al.*, "Mechanism for high hall-effect mobility in sputtered-MoS2 film controlling particle energy," in *Proc. S3S Conf.*, Burlingame, CA, USA, 2018, pp. 1–2, doi: 10.1109/S3S.2018.8640168.

[16] K. Matsuura *et al.*, "Low-carrier-density sputtered MoS_2 film by vapor-phase sulfurization," *J. Electron. Mater.*, vol. 47, no. 7, pp. 3497–3501, Mar. 2018, doi: 10.1007/s11664-018-6191-z.

[17] M. Hamada *et al.*, "High hall-effect mobility of large-area atomic-layered polycrystalline ZrS_2 film using UHV RF magnetron sputtering and sulfurization," *IEEE J. Electron Devices Soc.*, vol. 7, pp. 1258–1263, 2019, doi: 10.1109/JEDS.2019.2943609.

[18] S. Imai *et al.*, "Importance of crystallinity improvement in MoS_2 film by compound sputtering even followed by post sulfurization," *Jpn. J. Appl. Phys.*, vol. 60, p. SBBH10, Feb. 2021, doi: 10.35848/1347-4065/abdcae.

[19] K. Matsuura *et al.*, "Normally-off sputtered-MoS_2 *n*MISFETs with TiN top-gate electrode all defined by optical lithography for chip-level integration," *Jpn. J. Appl. Phys.*, vol. 59, no. 8, Aug. 2020, Art. no. 080906, doi: 10.35848/1347-4065/aba9a3.

[20] M. Hamada *et al.*, "ZrS_2 symmetrical-ambipolar FETs with near-midgap TiN film for both top-gate electrode and Schottky-barrier contact," *Jpn. J. Appl. Phys.*, vol. 60, p. SBBH05, Jan. 2021, doi: 10.35848/1347-4065/abd6d7.

[21] T. Hamada *et al.*, "WS2pMISFETs by sputtering and sulfur-vapor annealing with TiN/HfO2-top-gate-stack, TiN contact and ultra-thin body and box," in *Proc. 5th IEEE Electron Devices Technol. Manuf. Conf. (EDTM)*, Chengdu, China, 2021, pp. 1–3, doi: 10.1109/EDTM50988.2021.9420925.

[22] R. Tsuchiya *et al.*, "Controllable inverter delay and suppressing Vth fluctuation technology in silicon on thin BOX featuring dual back-gate bias architecture," in *Proc. IEEE Int. Electron Devices Meeting*, Washington, DC, USA, 2007, pp. 475–478, doi: 10.1109/IEDM.2007.4418977.

[23] A. Kranti, S. Burignat, J.-P. Raskin, and G. A. Armstrong, "Underlap channel UTBB MOSFETs for low—Power analog/RF applications," in *Proc. 10th Int. Conf. Ultimate Integr. Silicon*, Aachen, Germany, 2009, pp. 173–176, doi: 10.1109/ULIS.2009.4897564.

[24] H. Tanigawa *et al.*, "Enhancement-mode accumulation capacitance–voltage characteristics in TiN/ALD-Al_2O_3/sputtered-MoS_2 top-gated stacks," *Jpn. J. Appl. Phys.*, vol. 59, p. SMMC01, Apr. 2020, doi: 10.35848/1347-4065/ab7fea.

[25] S. Salehi and A. Saffarzadeh, "Atomic defect states in monolayers of MoS_2 and WS_2," *Surface Sci.*, vol. 651, pp. 215–221, Sep. 2016, doi: 10.1016/j.susc.2016.05.003.

[26] L. Yang *et al.*, "Chloride molecular doping technique on 2D materials: WS_2 and MoS_2," *Nano Lett.*, vol. 14, no. 11, pp. 6275–6280, Oct. 2014, doi: 10.1021/nl502603d.

[27] B. Tang *et al.*, "Direct n- to p-type channel conversion in monolayer/few-layer WS_2 field-effect transistors by atomic nitrogen treatment," *ACS Nano*, vol. 12, no. 3, pp. 2506–2513, Mar. 2018, doi: 10.1021/acsnano.7b08261.

[28] C. Tian and S. W. Chan, "Electrical conductivities $(CeO_2)_{1-x}(Y_2O_3)_x$ of thin films," *J. Am. Ceram. Soc.*, vol. 85, no, 9, pp. 2222–2229, Dec. 2004, doi: 10.1111/j.1151-2916.2002.tb00439.x.

[29] H. Qiu *et al.*, "Hopping transport through defect-induced localized states in molybdenum disulphide," *Nat. Commun.*, vol. 4, no. 1, pp. 1–6, Dec. 2014, doi: 10.1038/ncomms3642.

[30] S. Shin, Z. Jin, D. H. Kwon, R. Bose, and Y.-S. Min, "High turnover frequency of hydrogen evolution reaction on amorphous MoS_2 thin film directly grown by atomic layer deposition," *Langmuir*, vol. 31, no, 3, pp. 1196–1202, Oct. 2015, doi: 10.1021/la504162u.

[31] F. Wang *et al.*, "Uncovering the conduction behavior of van der Waals ambipolar semiconductors," *Adv. Mater.*, vol. 31, no. 1, Jan. 2019, Art. no. 1805317, doi: 10.1002/adma.201805317.

[32] Y. Guo and J. Robertson, "Band engineering in transition metal dichalcogenides: Stacked versus lateral heterostructures," *Appl. Phys. Lett.*, vol. 108, no. 23, Jun. 2016, Art. no. 233104, doi: 10.1063/1.4953169.

[33] K. Terada, "Measurement errors in effective channel-length extraction," *Electron. Commun. Jpn. II, Electron.*, vol. 79, no. 1, pp. 43–50, 1996, doi: 10.1002/ecjb.4420790105.

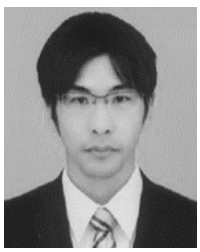

TAKUYA HAMADA received the M.E. degree in electrical engineering from the Tokyo Institute of Technology, Japan, in 2019, where he is currently pursuing the Doctoral degree.

MASAYA HAMADA received the M.E. degree in electrical engineering from the Tokyo Institute of Technology, Japan, in 2019, where he is currently pursuing the Doctoral degree.

SATOSHI IGARASHI received the B.E. and M.E. degrees in electrical engineering from the Tokyo Institute of Technology, Japan, in 2019, and 2021, respectively.

TAIGA HORIGUCHI received the B.E. degree in electrical engineering from the Tokyo Institute of Technology, Japan, in 2020, where he is currently pursuing the master's degree.

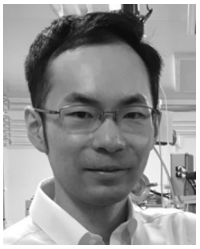

IRIYA MUNETA (Member, IEEE) received the B.E., M.E., and Ph.D. degrees in engineering from the University of Tokyo, Japan, in 2009, 2011, and 2014, respectively, where he worked as a Postdoctoral Researcher for two years. During this period, he focused on molecular beam epitaxy, materials science, and electronic devices based on ferromagnetic semiconductors. He joined the Tokyo Institute of Technology, Japan, in 2016, where he is currently an Assistant Professor. His current research is focused on 2-D materials and transition-metal di-chalcogenides, particularly the deposition of thin films, materials science, and their integration in devices.

KUNIYUKI KAKUSHIMA (Member, IEEE) received the B.S., M.S., and Ph.D. degrees in electrical engineering from the University of Tokyo, Japan, in 1999, 2001, and 2004, respectively.

He is currently an Associate Professor with the Tokyo Institute of Technology, Yokohama, Japan.

KAZUO TSUTSUI (Senior Member, IEEE) received the B.E., M.E., and Ph.D. degrees in electrical engineering from the Tokyo Institute of Technology, Japan, in 1981, 1983, and 1986, respectively.

He was with the Tokyo Institute of Technology as a Research Associate with the Department of Physical Electronics and the Department of Applied Electronics from 1986 to 1990, and as an Associate Professor with the Department of Applied Electronics from 1990 to 2010, where he is currently a Professor with the Institute of Innovative Research. His research interests include semiconductor electron devices, process technologies, and related characterization. He is a Fellow of the Japanese Society of Applied Physics, a Senior Member of the IEEE Electron Device Society, and a member of the Electrochemical Society and the Institute of Electronics, Information, and Communication Engineers.

TETSUYA TATSUMI received the B.S. and M.S. degrees from Waseda University in 1987 and 1989, respectively, and the Ph.D. degree from Keio University in 2000.

He joined Sony Corporation in 1989 and was engaged in the development of plasma technology for various semiconductor devices. He was a member of the Association for Super Advanced Electronics Technology from 1997 to 2001, where he led basic research on dry etching plasma. He is currently a Distinguished Engineer with Sony Semiconductor Solutions Corporation and a specially appointed Professor with the Tokyo Institute of Technology. He was awarded a Fellow of the Japanese Society of Applied Physics in 2015.

SHIGETAKA TOMIYA received the B.S. and M.S. degrees in physics and the Ph.D. degree in electronics engineering from Keio University, Japan, in 1986, 1988, and 1999, respectively.

In 1988, he joined the Sony Corporation Research Center, Yokohama, Japan. He has been engaged in the material analysis of wide bandgap compound semiconductors and the development of optical devices. He was a Visiting Researcher with the University of California at Santa Barbara, from 1991 to 1992, where he investigated novel quantum structures. Since then, he has been engaged in the development of various electronic material systems for sensors and compound semiconductor optical/electron devices. He is currently a Distinguished Researcher of Sony Corporation, Atsugi, Japan, and is a specially appointed Professor with the Tokyo Institute of Technology, Yokohama. He served as the Vice-Chair of the Committee of Manufacturing Process Innovation by Materials Informatics, JSPS, from 2016 to 2019. He currently serves as the Section Chief of the Hybrid Quantum-Nanotechnology Committee, JSPS.

HITOSHI WAKABAYASHI (Senior Member, IEEE) received the M.E. and Ph.D. degrees in electrical engineering from the Tokyo Institute of Technology, Japan, in 1993 and 2003, respectively.

He was with the NEC Corporation from 1993 to 2006, Massachusetts Institute of Technology from 2000 to 2001, and Sony Corporation from 2006 to 2012. He has been with the Tokyo Institute of Technology since 2013. He was a recipient of JSAP's Young Scientist Presentation Award in 2000. He has served as the Chair of the VLSI Technology and Circuits Committee, EDS, and the General Chair for the Symposium on VLSI Technology 2013, EDTM 2018, and IWJT 2017, 2019, and 2021.